

**Measurements and Simulations of Nadir-Viewing Radar Returns  
from the Melting Layer at X- and W-Bands**

Liang Liao

Goddard Earth Sciences & Technology Center/UMBC, Greenbelt, MD 20771

Robert Meneghini

Code 613.1, NASA/GSFC, Greenbelt, MD 20771

Lin Tian

Goddard Earth Sciences & Technology Center/UMBC, Greenbelt, MD 20771

Gerald M. Heymsfield

Code 613.1, NASA/GSFC, Greenbelt, MD 20771

Submitted to

Journal of Applied Meteorology and Climatology

**Corresponding author information:**

**Dr. Liang Liao**

Goddard Earth Science Technology/UMBC

Code 613.1

NASA/Goddard Space Flight Center

Greenbelt, MD 20771

301-614-5718 (phone)

301-614-5558 (fax)

Email: [Liang.Liao-1@nasa.gov](mailto:Liang.Liao-1@nasa.gov)

## Abstract

Simulated radar signatures within the melting layer in stratiform rain, namely the radar bright band, are checked by means of comparisons with simultaneous measurements of the bright band made by the EDOP (X-band) and CRS (W-band) airborne Doppler radars during the CRYSTAL-FACE campaign in 2002. A stratified-sphere model, allowing the fractional water content to vary along the radius of the particle, is used to compute the scattering properties of individual melting snowflakes. Using the effective dielectric constants computed by the conjugate gradient-fast Fourier transform (CGFFT) numerical method for X and W bands, and expressing the fractional water content of melting particle as an exponential function in particle radius, it is found that at X band the simulated radar bright-band profiles are in an excellent agreement with the measured profiles. It is also found that the simulated W-band profiles usually resemble the shapes of the measured bright-band profiles even though persistent offsets between them are present. These offsets, however, can be explained by the attenuation caused by cloud water and water vapor at W band. This is confirmed by the comparisons of the radar profiles made in the rain regions where the un-attenuated W-band reflectivity profiles can be estimated through the X- and W-band Doppler velocity measurements. The bright-band model described in this paper has the potential to be used effectively for both radar and radiometer algorithms relevant to the TRMM and GPM satellite missions

## 1. Introduction

The bright band, a layer of enhanced radar echo associated with melting hydrometeors, is often observed in stratiform rain. Understanding the microphysical properties of melting hydrometeors and their scattering and propagation effects is of great importance in accurately estimating parameters of the precipitation from spaceborne radar and radiometers (Bringi et al. 1986; Fabry and Szymer 1999; Olsen et al., 2001a and 2001b; Meneghini and Liao 2000; Liao and Meneghini 2005; Sassen et al., 2005 and 2007;). These instruments include the Precipitation Radar (PR) and the TRMM Microwave Imager (TMI) on the Tropical Rainfall Measuring Mission (TRMM) and the Dual-wavelength Precipitation Radar (DPR) and GPM Microwave Imager (GMI) on the proposed Global Precipitation Measuring (GPM). However, one of the most difficult problems in the study of the radar signature of the melting layer is the determination of the effective dielectric constants of melting hydrometeors. Although a number of mixing formulas are available to compute the effective dielectric constants, their results vary to a great extent when water is involved in the mixture, such as in the case of melting snow. It is physically unclear as to how to select among these various formulas (Meneghini and Liao 1996).

Although some success was achieved in simulating the radar bright-band signatures from the TRMM Precipitation Radar (Ku band) and airborne dual-wavelength radar (X and Ka bands) by modeling melting snow as a stratified sphere, a sphere composed of multiple layers (Liao and Meneghini 2005), the accuracy of the formulation needs to be examined in greater detail at other radar frequencies. Simultaneous measurements of the bright band made by the EDOP (X-band) and CRS (W-band) airborne Doppler radars during the CRYSTAL-FACE campaign in 2002 provide an excellent opportunity to check the validity of the stratified-sphere scattering model. Measurements of both radar reflectivities and Doppler velocities at two frequencies with the

higher frequency at W-band are particularly useful for testing the model. In the stratified-sphere model the water fraction is constant within each layer of the stratified sphere but is allowed to vary from layer to layer. As such, the stratified-sphere scattering model, which was described in detail by Wu and Wang (1991), can be used to compute scattering parameters for non-uniformly melting hydrometeors where the fractional water content is prescribed as a function of the particle radius. A melting layer model provides the melting fractions and fall velocities of hydrometeors as a function of the distance from the  $0^{\circ}$  C isotherm. By coupling this information with snow mass density, particle size distribution, and the effective dielectric constants of the mixed-phase hydrometeors, the backscattering intensities and attenuation coefficients can be computed from any location within the melting region.

The paper is organized as follows. In Section 2 we derive the effective dielectric constants of uniformly mixed snow and water particles from their internal electric fields by using the computational model in which the particles are described by a collection of  $128 \times 128 \times 128$  cubic cells of identical size and the CGFFT (Conjugate Gradient Fast Fourier Transform) numerical method. Procedures to simulate the radar bright-band signatures using the stratified-sphere model are described in Section 3. Comparisons of the simulated radar profiles in the melting layer of the EDOP and CRS airborne measurements are given in Section 4 followed by the summary in Section 5.

## 2. Effective Dielectric Constant

Let  $\mathbf{E}(\mathbf{r}, \lambda)$  and  $\mathbf{D}(\mathbf{r}, \lambda)$  be the local electric and dielectric displacement fields within a composite material at location  $\mathbf{r}$  at free-space wavelength  $\lambda$ , satisfying

$$\mathbf{D}(\mathbf{r}, \lambda) = \varepsilon(\mathbf{r}, \lambda)\mathbf{E}(\mathbf{r}, \lambda), \quad (1)$$

where  $\epsilon$  is the dielectric constant. In view of the local constitutive law described by the above equation, the bulk effective dielectric constant,  $\epsilon_{\text{eff}}$ , is defined as the ratio of the volume averages of  $D$  and  $E$  fields (Stroud and Pan 1978)

$$\epsilon_{\text{eff}} \iiint_V \mathbf{E}(\mathbf{r}, \lambda) d\mathbf{v} = \iiint_V \mathbf{D}(\mathbf{r}, \lambda) d\mathbf{v} \quad (2)$$

If the particle, composed of two materials  $\epsilon_1$  and  $\epsilon_2$ , is approximated by  $N$  small equal-volume elements, then the  $\epsilon_{\text{eff}}$  can be written as

$$\epsilon_{\text{eff}} = \frac{\epsilon_1 \sum_{j \in M_1} \mathbf{E}_j + \epsilon_2 \sum_{j \in M_2} \mathbf{E}_j}{\sum_{j \in M_1} \mathbf{E}_j + \sum_{j \in M_2} \mathbf{E}_j} \quad (3)$$

The notations  $\sum_{j \in M_1}$  and  $\sum_{j \in M_2}$  denote summations over all volume elements comprising materials 1 and 2, respectively. In this study, the internal fields appearing on the right-hand sides of (3) are computed by the CGFFT numerical procedure in which the volume enclosing the total particle is divided into  $128 \times 128 \times 128$  identical cells. Validation of the computational procedures for  $\epsilon_{\text{eff}}$  has been extensively carried out for uniform and non-uniform snow-water mixtures (Meneghini and Liao, 1996 and 2000; Liao and Meneghini, 2005). This is done by comparing the scattering parameters, such as backscattering and extinction cross sections, and phase function, from realizations of the mixed-phase particle models with those from a uniform particle with dielectric constant  $\epsilon_{\text{eff}}$ . It has been shown that  $\epsilon_{\text{eff}}$  as derived from (3) is sufficiently accurate to compute the effective dielectric constant of snow and water mixtures in the microwave range. An example of a realization of a uniformly mixed snow-water particle is shown in Fig.1 for a water fraction of 0.3. The dark and light gray areas represent water and snow, respectively. The minimum size of any snow or water region is chosen to be at least  $4 \times 4 \times 4$  cells to better satisfy the boundary conditions at the snow-water interfaces.

Figures 2 and 3 display the real and imaginary parts of  $\epsilon_{\text{eff}}$  of uniformly mixed snow-water hydrometeors versus water fractions at X and W bands as computed from (3) by the CGFFT for a snow density of  $0.1 \text{ g/cm}^3$ . For comparison, the results from the Maxwell Garnett (1904) and the Bruggeman (1935) mixing formulas are also shown in the plots. As can be seen in Figs. 2 and 3, the results of  $\epsilon_{\text{eff}}$  derived from the CGFFT lie between the two results derived from the Maxwell Garnett mixing formula, one in which water is treated as the matrix with snow inclusions ( $\text{MG}_{\text{WS}}$ ), and the other in which the roles of water and snow are reversed, i.e., snow as matrix and water as inclusion ( $\text{MG}_{\text{SW}}$ ). The results of the Bruggeman (1935) mixing formula are bounded within the results of  $\text{MG}_{\text{WS}}$  and  $\text{MG}_{\text{SW}}$ , but tend to yield larger real and imaginary parts of  $\epsilon_{\text{eff}}$  than the CGFFT.

### 3. Bright-Band Simulations

To simulate the radar signatures in the melting layer, two models are required: One is the melting layer model that provides microphysical properties of the mixed-phase hydrometeors, such as melting fractions and fall velocities of individual hydrometeors over their size spectra, as a function of the distance from  $0^\circ\text{C}$  isotherm; the other is the particle scattering model that is used to compute the scattering properties of the melting hydrometeors. Using the information provided by the melting layer model along with the particle scattering model, snow mass density and particle size distribution, the backscattering intensities and attenuation coefficients can be computed from any location within the melting region. In this study, the snow is assumed to fall and melt in accordance with the model described by Yokoyama and Tanaka (1984). Aggregation and drop breakup are not included in the model. Although there are many studies on importance of aggregation and drop breakup in the melting layer, their results vary (Yokoyama 1984; Mitra

et al. 1990; Szyrmer and Zawadzki 1999). The one-to-one correspondence between snow particles and raindrops is suggested by the field observations of Du Toit (1967) and Ohtake (1969). Long-term radar observations of weak and moderately intense bright bands by Fabry and Zawadzki (1995) indicate that the combined effect of aggregation and breakup, though present, on the average accounts for less than 1 dB of change in reflectivity from snow above to rain below the melting layer.

The mass density of snowflakes, as noted above, is among a few parameters that affect simulations of radar bright band profiles. Several studies reveal that snow density varies with its size and possibly changes as melting progresses (Nakaya 1954; Magono and Nakamura 1965; Zikmunda and Vali 1972; Locatelli and Hobbs 1974; Brandes et al. 2007). However, the results exhibit a great deal of variability depending on snow type, amount of riming and other conditions under which the studies were done. Moreover, there is a great uncertainty in determining a general relationship between snow density and fall velocity. This poses difficulties in specifying these variables and in carrying out the melting layer simulations. Because of these difficulties we use constant snow density, independent of particle size and fractional melt water. Varying the snow density as a function of its size and melting stage tends to improve the physics of the model (Zawadzki et al. 2005; Ryzhkov et al. 2007) but at the expense of more complicated computations and a greater number of free parameters. Because of these uncertainties and because the fixed snow density assumption yields reasonable results, we will not consider the variable snow density case in this paper.

To model the fact that melting usually starts at the particle surface and then progresses toward the center (Fujiyoshi, 1986), we employ the stratified-sphere particle model, which consists of 100 concentric equal-thickness layers. The melting water distribution or fractional

water content inside the particle can be expressed as a function of radius. Within each layer of the stratified sphere the effective dielectric constant is fixed and determined from the results of Figs.2 and 3 (X and W bands, respectively) based on the fractional water content specified at the layer of interest. An exponential function is adopted to describe the fractional water content  $f_w$  in terms of radius  $r$

$$f_w(r) = \begin{cases} f_w(0)e^{\frac{\beta r}{r_0}}, & r < r' \\ 1, & r_0 \geq r > r' \end{cases} \quad (4)$$

where  $r_0$  is the radius of the particle, and  $r'$  is the radius at which  $f_w$  is equal to 1, i.e.,  $f_w(r')=1$ . The coefficient  $\beta$  specifies the radial gradient of the water fraction so that a larger  $\beta$  results in a more rapid transition from snow to water. Its value was found to be 4.5 from the simulation study reported by Liao and Meneghini (2005). An example of such stratified-sphere models of melting snow for volume-averaged water fraction  $F_w$  of 0.1, 0.2 and 0.3 are shown in Fig.4.

To model the bright-band reflectivity the Marshall±Palmer raindrop size distribution (1948),  $N(D)$  in  $m^{-3}mm^{-1}$ , is assumed, which can be expressed as a function of rain rate,  $R$  in mm/h, by

$$N(D) = 8000\exp(-4.1R^{-0.21}D), \quad (5)$$

where  $D$  is diameter of particle in mm. The form of the  $Z_e$ - $R$  relation at X band, assuming the Marshall-Palmer size distribution, is given by

$$Z_e = 290R^{1.6}. \quad (6)$$

At the range just below the melting layer,  $N(D)$  is obtained from the measured reflectivity at X band using (5) and (6). To maintain constant mass transport during fall of hydrometeors, the product of  $N(D)$  and particle velocity  $v(D)$  is fixed over the regions of snow, melting, and rain. This, in turn, provides estimates of  $N(D)$  in the snow and melting layers. Once  $N(D)$  has been



specified throughout the melting layer, the apparent or measured radar reflectivity factor,  $Z_m$  in  $\text{mm}^6/\text{m}^3$ , is determined at any range within the melting layer from the follow equation:

$$Z_m(\lambda, s) = Z_e(\lambda, s) \exp\left\{-0.2 \ln 10 \int_0^s [k_p(\lambda, s) + k_c(\lambda, s) + k_v(\lambda, s)] ds\right\}, \quad (7)$$

where  $\lambda$  is the wavelength, and the exponential term describes radar attenuation at a range of  $s$ .  $k_p$ ,  $k_c$  and  $k_v$  in dB/km are the specific attenuations from precipitation, cloud water, and water vapor, respectively. The precipitation may include rain, snow and mixed-phased hydrometeors, which can be computed by

$$k_p = 4.343 \times 10^{-3} \int_0^{\infty} N(D, s) \sigma_e(D, \lambda) ds, \quad (8)$$

where  $\sigma_e(D, \lambda)$  is the extinction cross section of particles. The true (un-attenuated) radar reflectivity factor is expressed as

$$Z_e(\lambda, s) = \frac{\lambda^4}{\pi^5 |K_w|^2} \int_0^{\infty} N(D, s) \sigma_b(D, \lambda) dD, \quad (9)$$

where  $\sigma_b(D, \lambda)$  is the backscattering cross section.  $K_w$  the dielectric factor, is used to designate  $(m^2-1)/(m^2+2)$ , where  $m$  is the complex refractive index of water. In this study,  $|K_w|^2$  is taken to be 0.93 at X band and 0.698 at W band. The computations of  $\sigma_b$  and  $\sigma_e$  depend upon the scattering model of hydrometeors and mixing formulas used in the determination of the effective dielectric constant of melting snow. The melting layer model of Yokoyama and Takana (1984) is used to produce a table that provides the water fractions and fall velocities of particles at each size bin as a function of distance from 0 °C isotherm. It should be noted that because of the lack of information on cloud water and water vapor, the attenuation corrections are only made for the precipitation.

Shown in Fig.5 are the simulated results of the X- and W-band radar profiles in the melting layer for the snow densities of 0.05, 0.1 and 0.2 g/cm<sup>3</sup> as computed from the melting layer model and stratified-sphere scattering model described above. In these simulations the Marshall-Palmer raindrop size distribution (1948) is assumed for a rain rate of 1.0 mm/h. The attenuation due to hydrometeors is also taken into account in the results. A change in the snow density has different impact on the results of the simulated bright-band profiles at X and W bands. The smallest snow density ( $\rho=0.05$  g/cm<sup>3</sup>) gives the biggest enhancement of the reflectivity at X band but yields the narrowest bright-band width. At W band no clear radar bright bands are seen in Fig.5, even though a strong enhancement in the radar reflectivity is apparent in the early stages of melting. In contrast to the results at X band, the biggest change in the radar reflectivity at W band from snow to the bright-band peak occurs at  $\rho=0.2$  g/cm<sup>3</sup>, the highest snow density among those used in the plot. After reaching the maximum, the radar reflectivities computed from all the values of the snow density tend to converge, and their intensities remain nearly constant up to the rain region. It should be noted that the primary difference in the bright-band signatures at these frequencies arises from the differences between Rayleigh (X-band) and non-Rayleigh scattering.

To see how the simulations vary with respect to the different mixing formulas, Fig.6 depicts the results of the simulated bright band computed from the Maxwell-Garnett (MG<sub>WS</sub> and MG<sub>SW</sub>) and the Bruggeman mixing formulas as well as the stratified-sphere model. The snow density is set to 0.1 g/cm<sup>3</sup>, and the rain rate is 1.0 mm/h for these computations. Comparisons of the results reveal that differences of the simulated profiles among these scattering models are quite distinctive at X band, in which the MG<sub>WS</sub> leads to the strongest bright-band peak, and its counterpart, MG<sub>SW</sub>, presents the weakest increase in reflectivity within the melting layer. The Bruggeman results show a moderate boost but still much less than those from the stratified-

sphere model. In contrast to X band, the simulated results at W band appear to be much less sensitive to the choice of mixing formula. All the profiles exhibit more or less the same behavior except that the reflectivity profile of  $MG_{WS}$  tends to rise more quickly than others and has a relatively small peak. The similarities of the simulated radar bright-band profiles at W band are largely due to the dominance of Mie scattering at W band and to the relatively small contrast of the dielectric constants for snow and water which results in a much smaller difference in the effective dielectric constants computed from the mixing formulas.

#### **4. Comparisons of Simulated Profiles to Measurements**

Comparisons of the simulated radar bright-band profiles to the measured ones offer a direct check of the models as to their validity and accuracy. Illustrated in Figs.7 and 8 are the measurements of the radar reflectivity factors and mean Doppler velocities by EDOP and CRS on 7 July 2002 from 20:15:00 UTC to 20:25:00 UTC during CRYSTAL-FACE. The EDOP and CRS, mounted on NASA ER-2 aircraft during the CRYSTAL-FACE field campaign, are the nadir-looking airborne Doppler radars operating at X and W bands respectively. A detailed description of the EDOP and CRS can be found in the literature (Heymsfield et al. 1996; Li et al. 2004). Vertical profiles are also plotted in Figs.7 and 8 at selected locations along the flight line. With a range resolution of 37.5 m, the signature of the bright band is clearly detected by both radars at an altitude of around 4 km throughout the flight line. To make the measured profiles less noisy, a smoothing procedure is used. This is done by first finding all the pairs of the X- and W-band profiles based on the criteria that the peaks of X-band within the melting layer are in the range of  $Z_{peak}$  to  $Z_{peak}+1$  (dB) (where  $Z_{peak}$  value is specified below), and then averaging the selected profiles separately for X and W bands. It is worth noting that with such procedure, the

stability of the measured radar mean profiles is dramatically improved. Shown in Fig.9 are the four EDOP (blue heavy-dotted lines) and CRS (red heavy-dotted lines) mean profiles that correspond to values of  $Z_{\text{peak}}$  of 30, 32, 34 and 37 dB where profiles with the lowest value are shown on the top-left panel and profiles with the highest value are shown on the bottom-right panel.

Using the stratified-sphere melting particle model described earlier and assuming the Marshall-Palmer size distribution for rain, the simulated radar profiles (solid lines) are computed and compared with the measured ones in Fig.9. The snow density used in our simulations is chosen as  $0.1 \text{ g/cm}^3$ , which is consistent with the findings of the previous study for the retrieval of the snow size distribution by use of dual-wavelength techniques for the same data (Liao et al., 2008). Because there is no particle breakup or aggregation assumed in the melting layer model, and also because the mass flux is constant within the melting layer, the particle size distribution (PSD) specified in rain can be uniquely converted to PSDs in the snow and melting layer regions. With the models being initialized in the way described earlier, the rain rate, which completely specifies the Marshall-Palmer size distribution, is the only free parameter in the simulation. In the comparisons depicted in Fig.9, the rain rates that give the best agreement between the simulated and measured profiles are 0.58, 0.88, 1.01 and 1.62 mm/h, respectively. As can be seen, the simulated radar bright bands are in excellent agreement with the measured ones at X band. They are not only matched well at the peaks of the bright band but also in the widths. Evaluating the comparisons at W band is not as straightforward as those at X band because of attenuation effects at W band. The chief contributors of attenuation at W band are cloud water and water vapor in addition to hydrometeors. Although attenuation by hydrometeors (snow, melting snow and rain) is taken into account in our simulations, the contributions from

cloud water and water vapor are not included. Since neither cloud water nor water vapor is detectable by the EDOP and CRS, and there are no independent measurements available in estimating them during the campaign, they are largely unknown. This, as a result, introduces uncertainties in the higher-frequency radar retrieval. As illustrated in Fig.9, the simulated profiles (solid) at W band tend to agree with the measured ones (dotted) in shape but offsets in the magnitudes are clearly seen. To determine whether these offsets can be attributed to cloud water and water vapor attenuations at W band, we conduct comparisons of attenuation-corrected radar profiles in rain between the model simulations and the reconstructed W-band profiles by use of Doppler measurements.

Taking an advantage of simultaneous measurements of the Doppler velocities at X and W bands, we can derive the un-attenuated or true W-band radar profiles in rain (Tian et al., 2007; Liao et al., 2008). The differential Doppler velocity (DDV), which is defined as the difference of the Doppler velocities between X and W bands, depends only on the particle median volume diameter ( $D_0$ ). This is also true of the radar dual-frequency ratio (DFR) in dB, which is equal to the difference of the radar reflectivity at X and W bands. However, in the case of the DFR, correction of attenuation due to hydrometeors, cloud water and water vapor must first be performed at W-band (assuming that attenuation at X band is negligible) whereas the DDV is independent of attenuation. Figure 10 depicts the relationships between DFR- $D_0$  (left) and DDV- $D_0$  (right), which are computed when the rain drop size distribution is given by the gamma distribution. The  $\mu$  in the plots is the shape factor of the gamma distribution, which is zero for the Marshall-Palmer size distribution (1948). Since the DDV is independent of the radar attenuation and also unaffected by air motion,  $D_0$  can be estimated from the measured DDV (Tian et al., 2007; Liao et al., 2008). This in turn leads to a value of DFR from the differential

Doppler-estimated  $D_0$ . The true radar reflectivity at W band is, by definition, the difference between the X-band reflectivity and the DFR, based on the assumption that attenuation at X band is negligible. This should be true for stratiform rain, particularly for the cases shown in Fig.9 where only light rain is present because of the fact that the specific attenuation in rain at X-band is about 0.02, 0.08 and 0.18 dB/km for a rain rate of 1.5, 5 and 10 mm/h, respectively, for the Marshall-Palmer raindrop size distribution. Note that the procedure used to obtain the DDV-derived estimate of the true reflectivity profile applies only to the rain and not the melting layer or snow. The diamond-shaped data points in Fig.9 represent the non-attenuated radar profiles of rain at W band, derived from the DDV. The dashed curves refer to the non-attenuated W-band radar profiles generated from the models. There is a fairly good agreement between the non-attenuated radar rain profiles generated from the model on one hand and the estimated results on the other, implying good accuracy in simulating the W-band bright-band profiles. We conclude that the differences between the simulated and measured W-band radar reflectivity profiles can be explained primarily by cloud water and water vapor contributions to the W-band attenuation, though the uncertainties in snow density, size distribution and fall velocity might contribute somewhat to the mismatch.

## 5. Summary

In simulation of the X- and W-band radar returns within the melting layer, a stratified-sphere model is used to describe non-uniformly melting of single snowflakes during their descent through the  $0^{\circ}$  isotherm. With use of the stratified-sphere particle model, the fractional water content is conveniently expressed as a function of the particle radius. As a result, the melting process, which starts at the snow surface and progresses to the center, can be realistically

modeled. In each layer of the stratified sphere, the fractional water content is constant but is allowed to change from layer to layer. The effective dielectric constant in the layer of interest is computed by the CGFFT numerical method in accordance with its specified fractional water content. Expressing the fractional water content as an exponential function in particle radius, and using Yokoyama and Tanaka melting layer model, the radar bright-band profiles are simulated and subsequently compared to the X- and W-band Doppler radar measurements. While excellent agreement is found at X band, there are persistent offsets between the model and measured results at W-band. These offsets, however, can be reasonably explained by the attenuation caused by cloud water and water vapor at W band. This is confirmed by the comparisons of the radar profiles made in the rain regions where the un-attenuated W-band reflectivity profiles can be estimated through the X- and W-band Doppler velocity measurements. It is shown that the simulated un-attenuated rain profiles at W band agree well with those from the retrieval of the Doppler measurements. Despite the difficulty in describing microphysical properties of hydrometeors in the melting layer, our simulations of the radar bright band made at X and W bands appear to be fairly accurate and suggest the usefulness of the stratified-sphere scattering model as well as the effective dielectric constants derived from mixed-phase particle realizations. The bright-band model described in this paper has the potential to be used effectively for both radar and radiometer algorithms relevant to the TRMM and GPM satellite missions.

## **ACKNOWLEDGEMENTS**

We wish to thank Dr. Lihua Li, Mr. Ed Zenker, Dr. Steven Bidwell and Dr. Paul Racette for EDOP and CRS data processing and engineering support. This work is supported by Dr. R.

Kakar of NASA Headquarters undHU □ 1\$6\$TV □ 3UHFLSLWDWLRQ □ 0HDVXUHPHQW □ 0LVVLRQ □ □

NNH06ZDA001N-PMM.



## References

- Bringi, V. N., R. M. Rasmussen, and J. Vivekanandan, 1986: Multiparameter radar measurements in Colorado convective storms. Part I: Graupel melting studies. *J. Atmos. Sci.*, **43**, 2545-2563.
- Brandes, E., K. Ikeda, G. Zhang, M. Schoenhuber, and R. Rasmussen, 2007: A statistical and physical description of hydrometeor distributions in Colorado snowstorms using a video distrometer. *J. Appl. Meteor. Climat.*, **46**, 634-650.
- Bruggeman, D. A. G., 1935: Berechnung verschiedener physikalischer Konstanten von heterogenen Substanzen: I. Dielectrizitatskonstanten und Leitfähigkeiten der Mischkörper aus isotropen Substanzen. *Ann. Phys.*, **24**, 636-679.
- Du Toit, P. S., 1967: Doppler radar observations of drop size in continuous rain. *J. Appl. Meteor.*, **6**, 1082-1087.
- Fabry, F., and I. Zawadzki, 1995: Long-term radar observations of the melting layer of precipitation and their interpretation. *J. Atmos. Sci.*, **52**, 838-851.
- Fabry, F. and W. Szymer, 1999: Modeling of the melting layer. Part II: Electromagnetics. *J. Atmos. Sci.*, **56**, 3596-3600.
- Fujiyoshi, Y., 1986: Melting snowflakes. *J. Atmos. Sci.*, **43**, 307-311.
- Gunn, K. L. S., and J.S. Marshall, 1958: The distribution with size of aggregate snowflakes. *J. Meteor.*, **15**, 452-461.
- Heymsfield, G. M., S. W. Bidwell, I. J. Caylor, S. Ameen, S. Nicholson, W. Bonczyk, L. Miller, D. Vandemark, P. E. Racette, and L. R. Dodd, 1996: The EDOP radar system on the high-altitude NASA ER-2 aircraft. *J. Atmos. Oceanic Technol.*, **13**, 795-809.
- Li, L. G. M., Heymsfield, P. E. Racette, L. Tian and E. Zenker, 2004: A 94-GHz cloud radar system on a NASA high-altitude ER-2 aircraft. *J. Atmos. Oceanic Technol.*, **21**, 1378-1488.
- Liao, L. and R. Meneghini, 2005: On modeling air/spaceborne radar returns in the melting layer. *IEEE Trans. Geosci. Remote Sens.*, **43**, 2799-2809.
- Liao, L., R. Meneghini, L. Tian, and G. M. Heymsfield, 2008: Retrieval of snow and rain from combined X- and W-band airborne radar measurements. *IEEE Trans. Geosci. Remote Sens.*, **46**, 1514-1524.
- Locatelli, J., and P. Hobbs, 1974: Fall speeds and masses of solid precipitation particles. *J. Geophys. Res.*, **79**, 2185-2197.

- Magono, C., and T. Nakamura, 1965: Aerodynamic studies of falling snowflakes. *J. Meteor. Soc. Japan*, **43**, 139-147.
- Marshall, J. S., and W.M. Palmer, 1948: The distribution of raindrops with size. *J. Appl. Meteor.*, **5**, 165-166.
- Maxwell Garnett, J. C., 1904: Colors in metal glasses and in metallic films. *Philos. Trans. R. Soc. London A*, **203**, 385-420.
- Meneghini, R. and L. Liao, 1996: Comparisons of cross sections for melting hydrometeors as derived from dielectric mixing formulas and a numerical method. *J. Appl. Meteorol.*, **35**, 1658-1670.
- Meneghini, R. and L. Liao, 2000: Effective dielectric constants of mixed-phase hydrometers. *J. Atmos. Oceanic Technol.*, **17**, 628-640.
- Mitra, S. K., O. Vohl, M. Ahr, and H. R. Pruppacher, 1990: A wind tunnel and theoretical study of the melting behavior of atmospheric ice particles. IV: Experiment and theory for snow flakes. *J. Atmos. Sci.*, **47**, 584-591.
- Nakaya, U., 1954: *Snow Crystals: Natural and Artificial*. Harvard University Press, 510pp.
- Ohtake, T., 1969: Observations of the size distribution of hydrometeors through the melting layer. *J. Atmos. Sci.*, **26**, 545-557.
- Olson, W. S., P. Bauer, N. F. Viltard, D. E. Johnson, W.-K. Tao, R. Meneghini, and L. Liao, 2001: A melting-layer model for passive/active microwave remote sensing applications. Part I: Model formulation and comparison with observations. *J. Appl. Meteorol.*, **40**, 1145-1163.
- Olson, W. S., P. Bauer, C. D. Kummerow, Y. Hong, and W.-K. Tao, 2001: A melting-layer model for passive/active microwave remote sensing applications. Part II: Simulations of TRMM observations. *J. Appl. Meteorol.*, **40**, 1164-1179.
- Ryzhkov, A., S. Giangrande, A. Khain, M. Pinsky, and A. Pokrovsky, 2008: Exploring model-based polarimetric retrieval of vertical profiles of precipitation. Proceedings of the 5<sup>th</sup> European Conference on Radar Meteorology, Finland.
- Sassen, K., J. R. Campbell, J. Zhu, P. Kollias, M. Shupe, and C. Williams, 2005: Lidar and triple-wavelength Doppler radar measurements of the melting layer: A revised model for dark and bright band phenomena. *J. Appl. Meteorol.*, **44**, 301-312.
- Sassen, K., S. Matrosov, and J. Campbell, 2007: CloudSat spaceborne 94 GHz radar bright bands in the melting layer: An attenuation-driven upside-down lidar analog. *Geophys. Res. Lett.*, **34**, L16818, doi:10.1029/2007GL030291.

- Stroud, D. and F. P. Pan, 1978: Self-consistent approach to electromagnetic wave propagation in composite media: Application to model granular metals. *Phys. Rev. B.*, **17**, 1602-1610.
- Szyrmer, W., and I. Zawadzki, 1999: Modeling of the melting layer. Part I: Dynamics and microphysics. *J. Atmos. Sci.*, **56**, 3573-3592.
- Tian, L., G. M. Heymsfield, L. Li, and R. Srivastava, 2007: Properties of light stratiform rain derived from 10 and 94 GHz airborne Doppler radars. *J. Geophys. Res.*, **112**, D11211, doi:10.1029/2006JD008144.
- Wu, Z. P., and Y. P. Wang, 1991: Electromagnetic scattering for multilayered sphere: Recursive algorithms. *Radio Sci.*, **2**, 1391-1401.
- Yokoyama, T. and H. Tanaka, 1984: Microphysical process of melting snowflakes detected by two-wavelength radar. Part I. Principle of measurement based on model calculation. *J. Meteorol. Soc. Jpn.*, **62**, 650-666.
- Yokoyama, T., H. Tanaka, K. Nakamura, and J. Awaka, 1984: Microphysical process of melting snowflakes detected by two-wavelength radar: Part II. Application of two-wavelength radar technique. *J. Meteorol. Soc. Jpn.*, **62**, 668-677.
- Zawadzki, I., W. Szyrmer, C. Bell, and F. Fabry, 2005: Modeling of the melting layer. Part III: The density effect. *J. Atmos. Sci.*, **62**, 3705-3723.
- Zikmunda, J., and G. Vali, 1972: Fall patterns and fall velocities of rimed ice crystals. *J. Atmos. Sci.*, **29**, 1334-1347.

## Figure Captions:

Fig.1 Realization of snow-water spherical particle at a water fraction of 0.3.

Fig.2 Comparisons of real (top) and imaginary (bottom) parts of  $\epsilon_{\text{eff}}$  for uniformly mixed snow-water spheres as derived from the CGFFT and several mixing formulas at X band.

Fig.3 Comparisons of real (top) and imaginary (bottom) parts of  $\epsilon_{\text{eff}}$  for uniformly mixed snow-water mixed spheres as derived from the CGFFT and several mixing formulas at W band.

Fig.4 Stratified-sphere models of melting snow for volume-averaged water fraction  $F_w$  of 0.1, 0.2 and 0.3 from Liao and Meneghini (2005).

Fig.5 Results of simulated radar profiles at X- and W-bands in the melting layer for snow densities ( $\rho$ ) of 0.05, 0.1 and 0.2  $\text{g/cm}^3$  using CGFFT stratified sphere model.

Fig.6 Comparison of simulated radar bright-band profiles at X- and W-bands as computed from the Maxwell-Garnett (MG) and Bragg (B) models for the snow density of 0.1  $\text{g/cm}^3$ .

Fig.7 Measured radar reflectivity factors (top and middle panels) from EDOP (X-band) and CRS (W-band) nadir-looking airborne radar over a 130-km flight line over stratiform rain. The selected radar reflectivity profiles in the locations given by the dashed lines are shown in the bottom panel where the red and blue curves represent the EDOP and CRS radar reflectivity profiles, respectively.

Fig.8 Measured mean Doppler velocities (top and middle panels) from EDOP (X-band) and CRS (W-band) for the same storm shown in Fig.6. The selected mean Doppler velocity profiles are shown in the bottom panel where the red and blue curves represent the EDOP and CRS, respectively.

Fig.9 Comparisons of simulated (solid) and measured (dotted) bright-band profiles at X (red) and W (blue) bands. The dashed lines are the simulated results without taking into account attenuation. The diamond-shaped data points are the estimated un-attenuated W-band profiles based on the Doppler measurements.

Fig.10 Plots of DFR vs.  $D_0$  (left) and DDV vs.  $D_0$  (right) for X- and W-band radars for rain as the shape factor ( $\mu$ ) of the gamma particle distribution varies from 0 to 6.

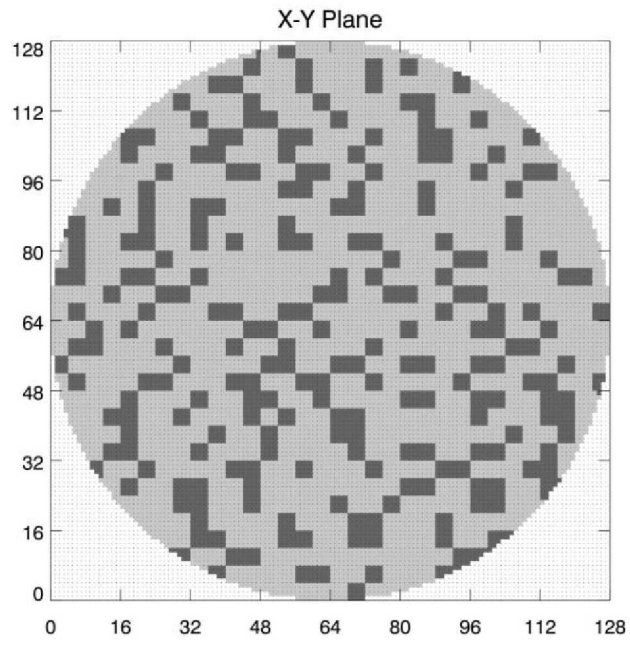


Fig.1 Realization of snow-water spherical particle at a water fraction of 0.3.

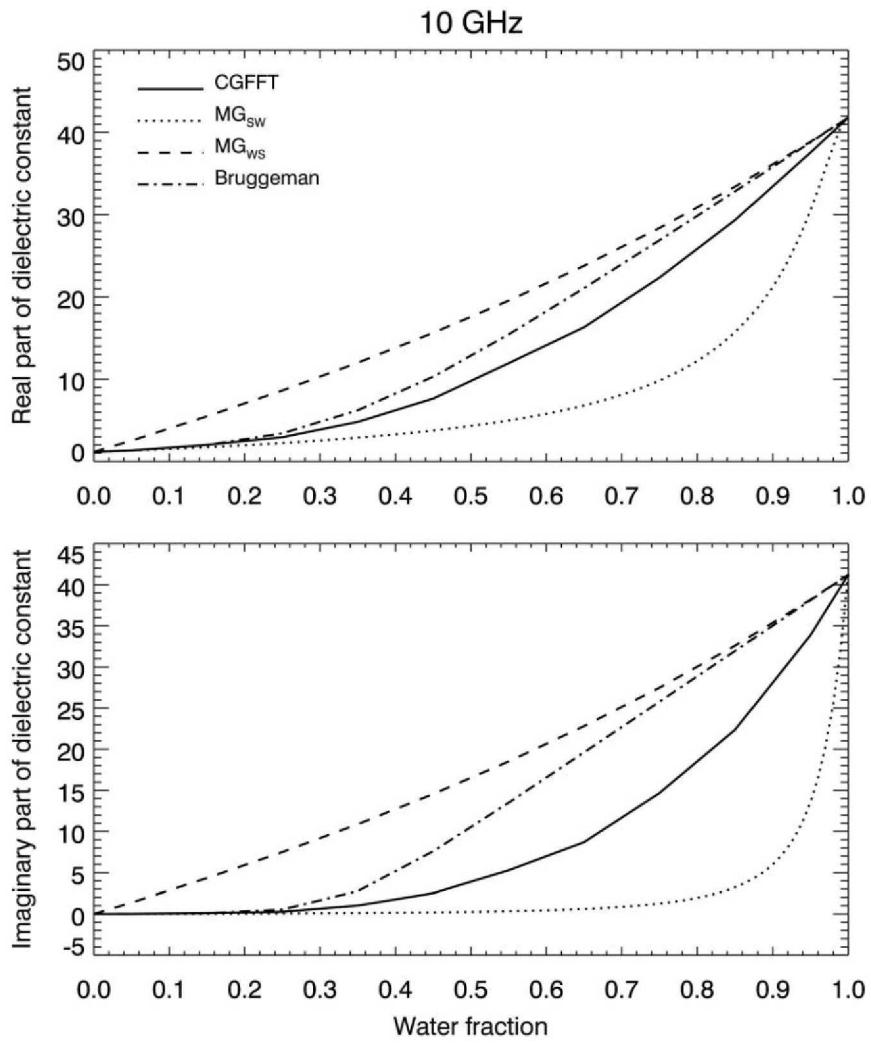


Fig.2 Comparisons of real (top) and imaginary (bottom) parts of  $\epsilon_{eff}$  for uniformly mixed snow-water spheres as derived from the CGFFT and several mixing formulas at X band.

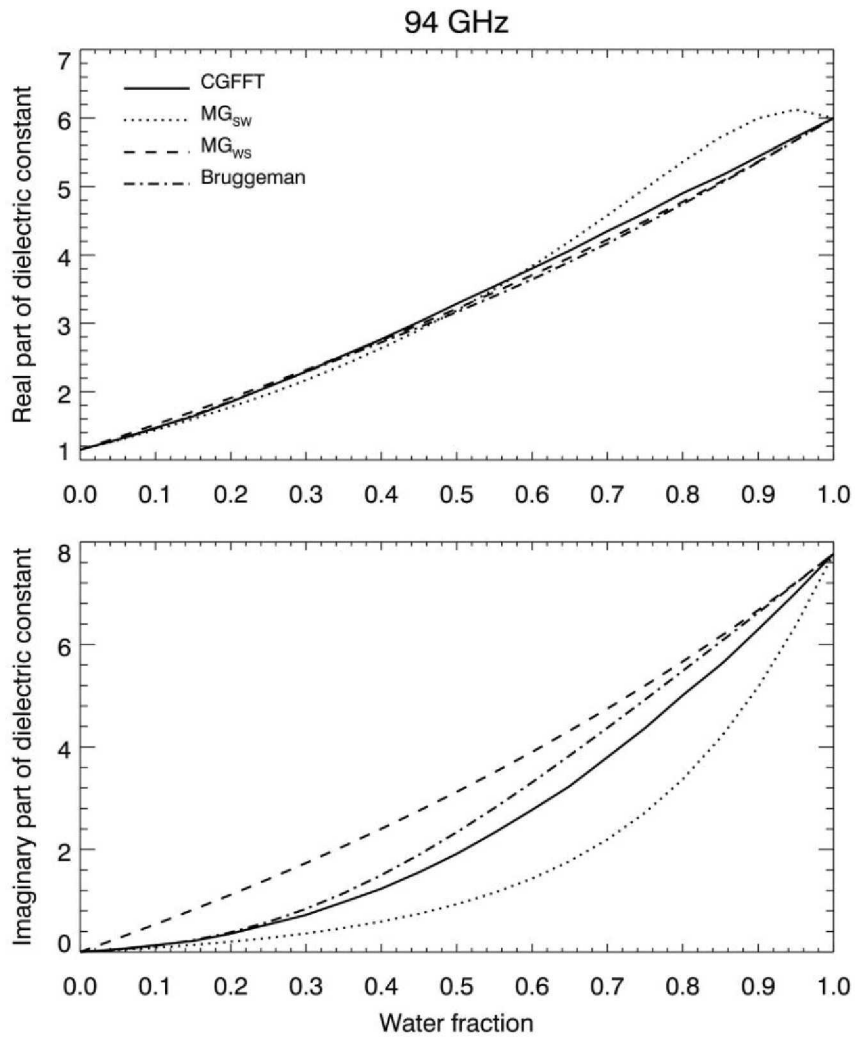


Fig.3 Comparisons of real (top) and imaginary (bottom) parts of  $\epsilon_{eff}$  for uniformly mixed snow-water mixed spheres as derived from the CGFFT and several mixing formulas at W band.

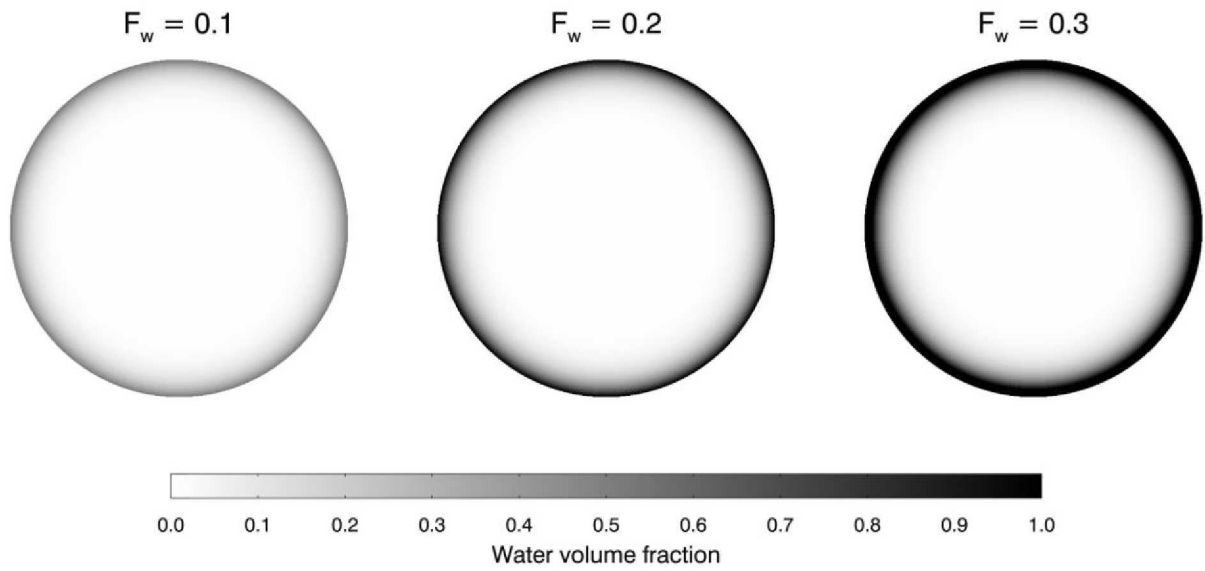


Fig.4 Stratified-sphere models of melting snow for volume-averaged water fraction  $F_w$  of 0.1, 0.2 and 0.3 from Liao and Meneghini (2005).



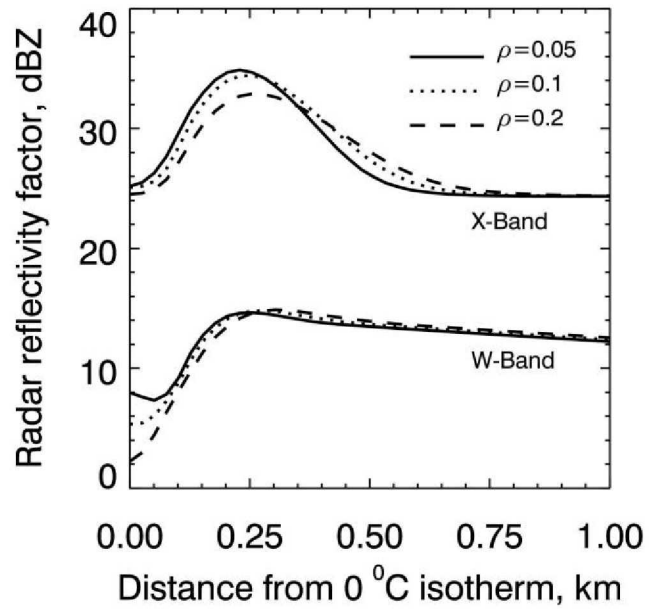


Fig.5 Results of simulated radar profiles at X- and W-bands in the melting layer for snow densities ( $\rho$ ) of 0.05, 0.1 and 0.2 g/cm<sup>3</sup> using CGFFT stratified sphere model.

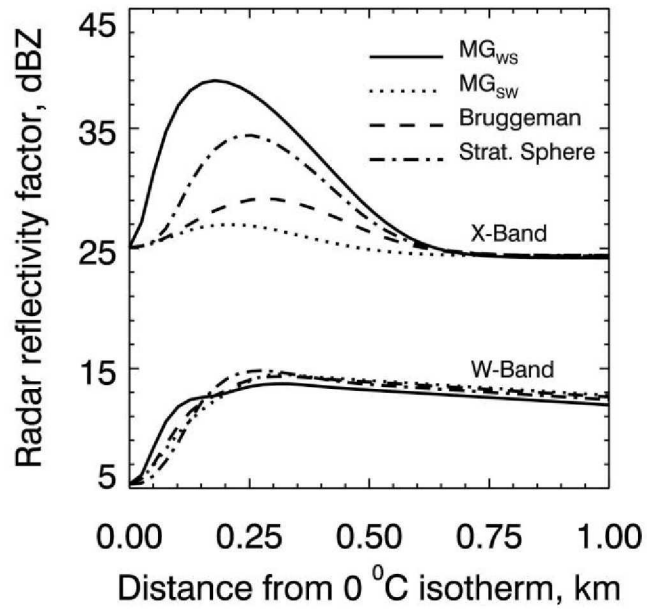


Fig.6 Comparison of simulated radar bright-band profiles at X- and W-bands as computed from the Maxwell-Garnett and Bruggeman mixing formulas as well as the stratified-sphere model for the snow density of  $0.1 \text{ g/cm}^3$ .

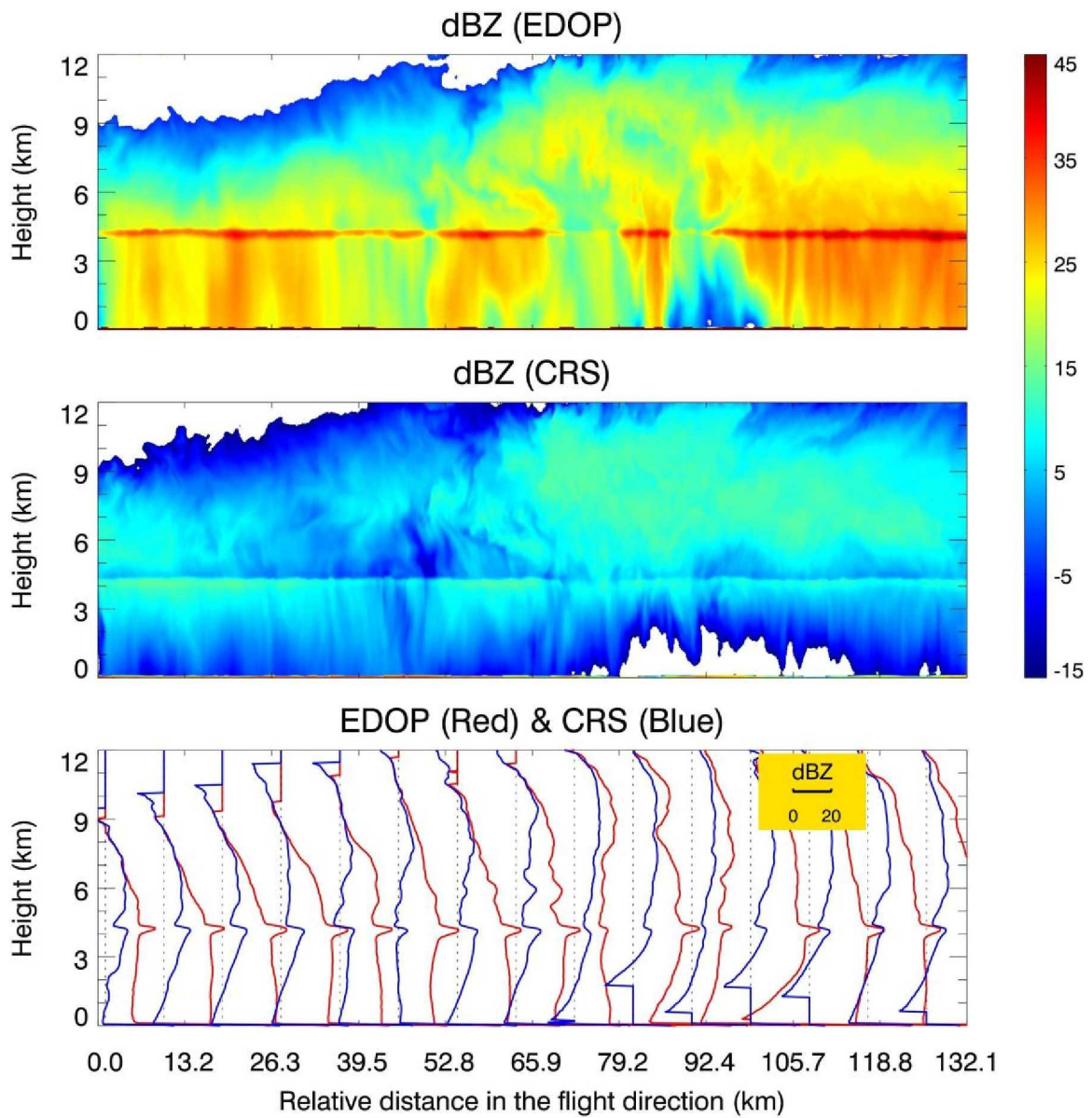


Fig.7 Measured radar reflectivity factors (top and middle panels) from the EDOP (X-band) and CRS (W-band) nadir-looking airborne radars over a 130-km flight line over stratiform rain. The selected radar reflectivity profiles in the locations given by the dashed lines are shown in the bottom panel where the red and blue curves represent the EDOP and CRS radar reflectivity profiles, respectively.

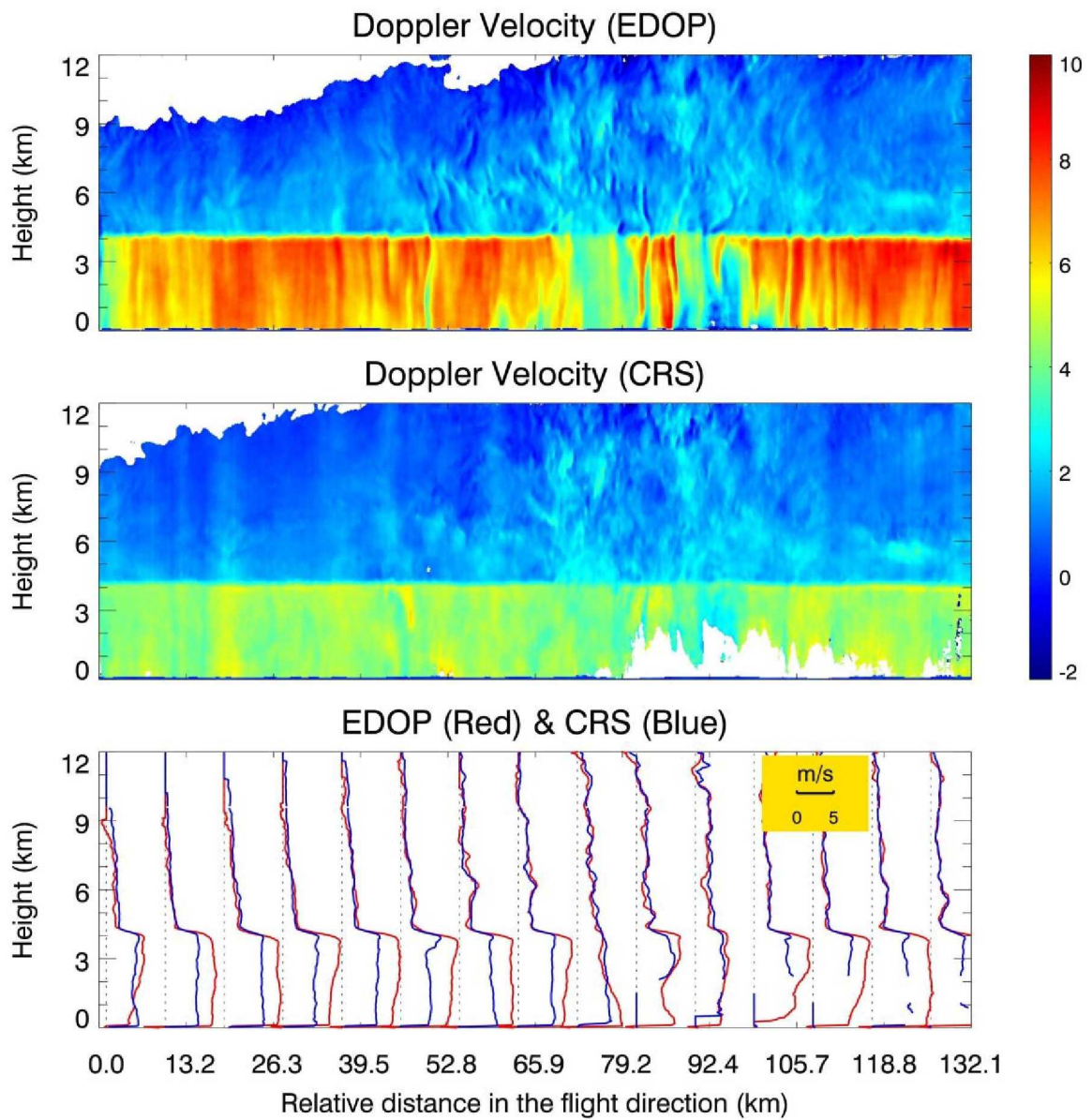


Fig.8 Measured mean Doppler velocities (top and middle panels) from EDOP (X-band) and CRS (W-band) for the same storm shown in Fig.6. The selected mean Doppler velocity profiles are shown in the bottom panel where the red and blue curves represent the EDOP and CRS, respectively.

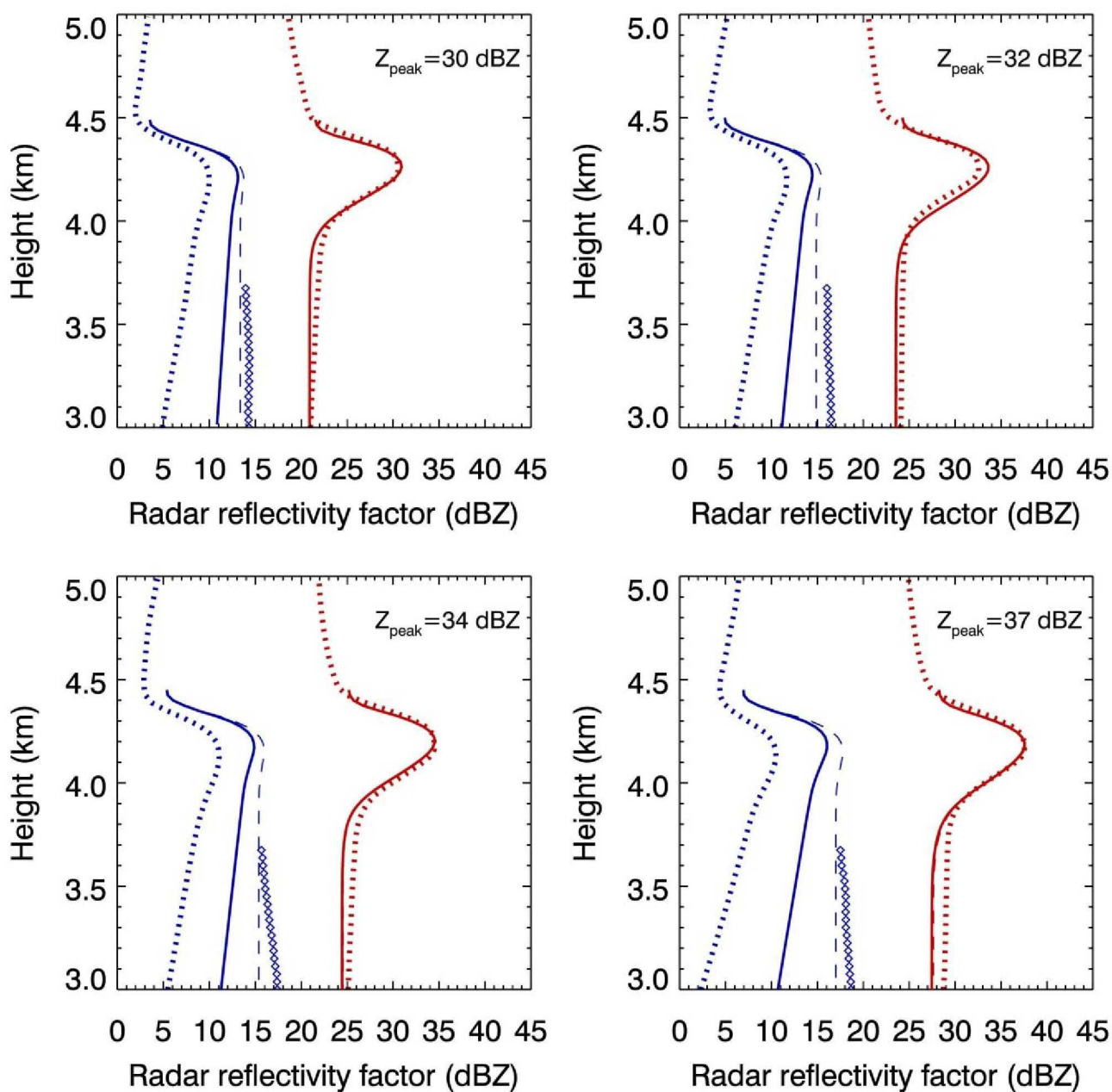


Fig.9 Comparisons of simulated (solid) and measured (dotted) bright-band profiles at X (red) and W (blue) bands. The dashed lines represent the simulated results without taking into account attenuation. The diamond-shaped data points represent the estimated un-attenuated W-band profiles based on the Doppler measurements.

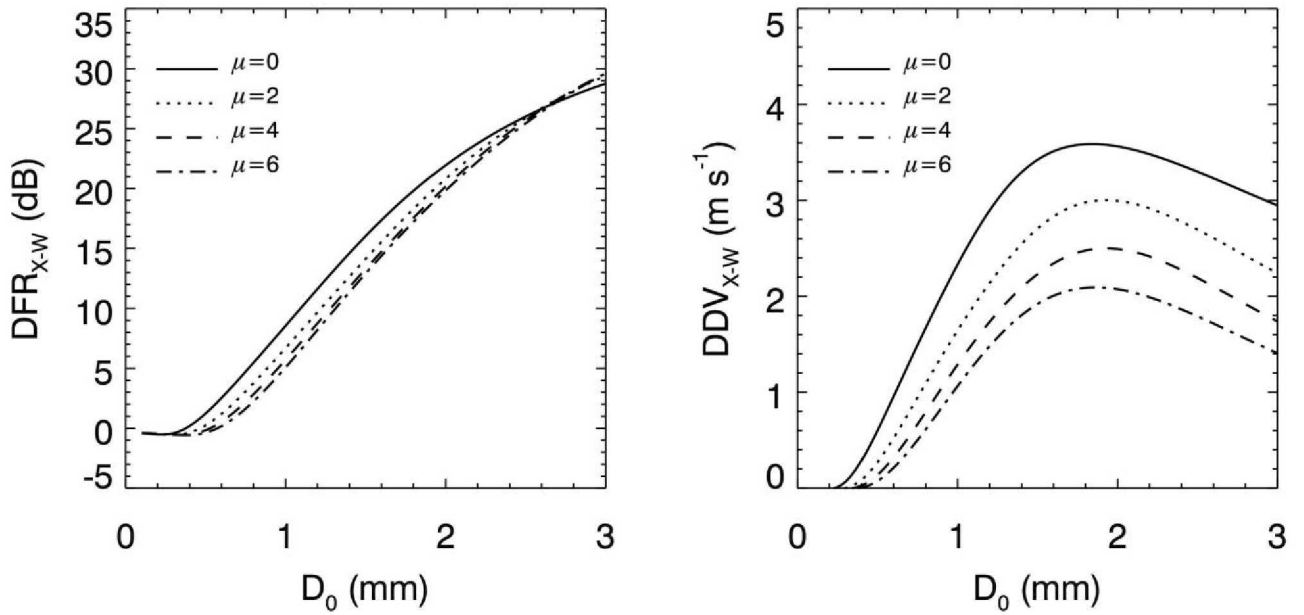


Fig.10 Plots of DFR vs.  $D_0$  (left) and DDV vs.  $D_0$  (right) for X- and W-band radars for rain as the shape factor ( $\mu$ ) of the gamma particle distribution varies from 0 to 6.

Liao, L., R. Meneghini, L. Tian, and G. M. Heymsfield, 2009: Measurements and simulations of nadir-viewing radar returns from the melting layer at X- and W-bands. *J. Appl. Meteor. Climat.*, **48**, 2215-2226.

### Abstract

Simulated radar signatures within the melting layer in stratiform rain, namely the radar bright band, are checked by means of comparisons with simultaneous measurements of the bright band made by the EDOP (X-band) and CRS (W-band) airborne Doppler radars during the CRYSTAL-FACE campaign in 2002. A stratified-sphere model, allowing the fractional water content to vary along the radius of the particle, is used to compute the scattering properties of individual melting snowflakes. Using the effective dielectric constants computed by the conjugate gradient-fast Fourier transform (CGFFT) numerical method for X and W bands, and expressing the fractional water content of melting particle as an exponential function in particle radius, it is found that at X band the simulated radar bright-band profiles are in an excellent agreement with the measured profiles. It is also found that the simulated W-band profiles usually resemble the shapes of the measured bright-band profiles even though persistent offsets between them are present. These offsets, however, can be explained by the attenuation caused by cloud water and water vapor at W band. This is confirmed by the comparisons of the radar profiles made in the rain regions where the un-attenuated W-band reflectivity profiles can be estimated through the X- and W-band Doppler velocity measurements. The bright-band model described in this paper has the potential to be used effectively for both radar and radiometer algorithms relevant to the TRMM and GPM satellite missions.